Engineering Failure Analysis 47 (2015) 328–337

Contents lists available at ScienceDirect

Engineering Failure Analysis

journal homepage: www.elsevier.com/locate/engfailanal

Surface nanodeformations caused by ultrashort laser pulse

N.A. Inogamov[a,*], V.V. Zhakhovsky[b,c], S.I. Ashitkov[c], Yu.N. Emirov[d], A.Ya. Faenov[c], Yu.V. Petrov[a], V.A. Khokhlov[a], M. Ishino[e], B.J. Demaske[b], M. Tanaka[e], N. Hasegawa[e], M. Nishikino[e], S. Tamotsu[f], T.A. Pikuz[c,e], I.Y. Skobelev[c], T. Ohba[e], T. Kaihori[e], Y. Ochi[e], T. Imazono[e], Y. Fukuda[e], M. Kando[e], Y. Kato[g], T. Kawachi[e], S.I. Anisimov[a], M.B. Agranat[c], I.I. Oleynik[b], V.E. Fortov[c]

[a] *Landau Institute for Theoretical Physics, Russian Academy of Sciences, Chernogolovka, Moscow Region 142432, Russian Federation*
[b] *Department of Physics, University of South Florida, Tampa, FL 33620, USA*
[c] *Joint Institute for High Temperatures, Russian Academy of Sciences, Moscow 125412, Russian Federation*
[d] *Nanomaterials and Nanomanufacturing Research Center, University of South Florida, Tampa, FL 33620, USA*
[e] *Quantum Beam Science Directorate, JAEA, Kizugawa, Kyoto 619-0215, Japan*
[f] *Graduate School of Humanities and Science, Nara Women's University, Nara 630-8506, Japan*
[g] *Graduate School for the Creation of New Photonics Industries, Hamamatsu 431-1202, Japan*

ARTICLE INFO

Article history:
Available online 30 January 2014

Keywords:
Nanometallurgy with ultrafast lasers
Mechanical action of X-ray and optical short pulse lasers
Laser nanospallation and nanostructuring

ABSTRACT

Ultrashort laser pulse is a unique nanometallurgical tool which operates at extreme conditions: ultimate strength of material, the smallest spatiotemporal scales, and nonequlibrium crystallization. Approaches to ultimate strength and to highly nonequlibrium crystallization are tightly coupled with the smallness of spatiotemporal scales. Usage of the tool opens new opportunities to create materials with enhanced surface hardness, anticorrosion properties, and diverted optical constants. To use these advantages we have first of all to develop clear and reliable physical model. The paper presents new results concerning interactions of optical or X-ray lasers with metals. It is shown that ultrashort laser pulse melts surface layer, sends shock into bulk, and foams molten metal. Dense dislocation bilayer is created thanks to fast recrystallization (the first sublayer) and plastic transformations behind strong shock (the second sublayer). Plastic shock generated at moderate laser intensities attenuates sharply during its propagation into metal. During this attenuation, a plastic shock regenerates into a powerful elastic shock. This process defines boundary between the second dislocation sublayer and undamaged solid. Mechanical breaking of foam after its strong stretching and fly away of a part of melt together with fast freezing are responsible for appearance of chaotic frozen nanostructures at an irradiated surface.

---

* Corresponding author. Tel.: +7 495 702 9317.

E-mail addresses: nailinogamov@gmail.com (N.A. Inogamov), vasily@usf.edu (V.V. Zhakhovsky), Ashitkov11@yandex.ru (S.I. Ashitkov), yemirov@fiu.edu (Yu.N. Emirov), anatolyf@hotmail.com (A.Ya. Faenov), uvp49@mail.ru (Yu.V. Petrov), v_a_kh@mail.ru (V.A. Khokhlov), ishino.masahiko@jaea.go.jp (M. Ishino), bdemaske@mail.usf.edu (B.J. Demaske), Momoko.Tanaka@jaea.go.jp (M. Tanaka), Noboru.Hasegawa@jaea.go.jp (N. Hasegawa), Masaharu.Nishikino@jaea.go.jp (M. Nishikino), tamotsu@cc.nara-wu.ac.jp (S. Tamotsu), tapikuz@mail.ru (T.A. Pikuz), skobelev@ihed.ras.ru (I.Y. Skobelev), Toshiyuki.Ohba@jaea.go.jp (T. Ohba), Takeshi.Kaihori@jaea.go.jp (T. Kaihori), Yoshihiro.Ochi@jaea.go.jp (Y. Ochi), Takashi.Imazono@jaea.go.jp (T. Imazono), fukuda.yuji@jaea.go.jp (Y. Fukuda), kando.masaki@jaea.go.jp (M. Kando), y.kato@gpi.ac.jp (Y. Kato), Tetsuya.Kawachi@jaea.go.jp (T. Kawachi), anisimov@itp.ac.ru (S.I. Anisimov), agranat2004@mail.ru (M.B. Agranat), oleynik@usf.edu (I.I. Oleynik), fortov@ihed.ras.ru (V.E. Fortov).

http://dx.doi.org/10.1016/j.engfailanal.2013.12.009
1350-6307/

1. Introduction

Let us shortly present mechanics of ultrafast irradiation. Short laser pulse from infrared to X-ray wavelength raises pressure in a thin surface layer. This pressurized layer decays acoustically into vacuum from the outer boundary of a target and into the bulk side of a target. The decay and corresponding expansion of matter of the pressurized layer produce tensile stress τ which stretches matter of this layer during acoustic decay time $t_s = d_T/c_s$, where d_T is thickness of the pressurized layer and c_s is speed of sound. Stress τ increases when absorbed energy F_{abs} increases. A spallation layer separates from a target if stress τ overcomes material strength τ_{str}. Simulations show that there is a molten layer with thickness $\sim d_T$, when an illumination is powerful enough to achieve the threshold condition $\tau = \tau_{str}$. Therefore nucleation of voids takes place in liquid. A spallation layer is located between a nucleation zone and vacuum boundary.

This layer does not separate immediately or shortly after nucleation if we compare the time period necessary for separation and hydrodynamic time scale t_s. In our case the thickness d_T of the spallation layer and its inertia (proportional to mass per unit of irradiated surface) are so small that after nucleation the significant deceleration of a spallation layer continues. This means that the cavitation bubbles continue to exist rather long time after their appearance in a nucleation process and therefore their walls continue to resist to stretching through surface tension. Huge stretching is necessary to break walls of bubbles. The content of liquid in a mixture decreases during stretching. Therefore small bubbles inside a volume of liquid (low content of vapor phase in vapor–liquid mixture) evolve into foam (low content of liquid phase in vapor–liquid mixture). There are two stages of deceleration of the target boundary [1,2]. At the first stage the boundary is decelerated by forces of resistance of condensed matter to stretching. This stage lasts up to beginning of nucleation of voids. At the second stage the boundary is decelerated by surface tension of bubbles. Spatiotemporal scales in the usual experiments with colliding plates are 0.1–1 cm and microsecond. Dynamically the second stage is insignificant in the case of the usual experiments where there is a thick spallation layer. While in our case with an extremely thin spallaton layer the role of the second stage strongly increases [1,2].

Near threshold $\tau = \tau_{str}$ the resisting stage is so long in time that cooling due to heat conduction into cold bulk of a target freezes the bubbles. The undersurface bubbles, frozen jets with drops at the ends of jets, and remnants of walls of broken bubbles form random nano-relief at a vacuum boundary of a target. The conclusion concerning the frozen undersurface bubbles follows from our recent experimental results and numerical simulations [1,2]. While the results concerning the jets, drops, and remnants are discussed below.

Newton rings have been presented in paper [3]. This observation has begun studies of expressly mechanical nature of ablation by ultrashort laser pulse (laser ablation is a process of matter removal as a result of laser irradiation). First explanation, why the interference rings appear, has been described in paper [4]. Let us introduce briefly physics of mechanical ablation. This will help better understand origin of surface nanostructures, since they are related to thermo-mechanical stretching of matter and fracture of spallation layer.

Geometry of a target, its vacuum boundary, and a surface layer $d_T(y)$ heated by absorption of a laser pulse – all they are shown in Fig. 1. The heated layer in our experiments is shallow since its normal (along the x-axis in Fig. 1) extension $d_T \sim$ 10–100 nm is much smaller than its radial size defined by radius $R_L \sim$ 10–100 µm of a laser beam. Laser pulse is short. Its duration is τ_L = 40 fs–10 ps. Laser heating initiates expansion of the heated layer d_T. This layer is shown in Fig. 1. At the ablation threshold F_{abl} [J/cm^2] voids nucleate at the nucleation depth $d_{\mathrm{crat}}|_{abl}$, $d_{crat}|_{abl} \sim \mathrm{d}_T$, see Fig. 2. Slightly above threshold F_{abl}, the radial extension $r_{nucl}|_{abl}$ of the nucleation disk is small in comparison with a beam radius R_L, see Figs. 1 and 2; the voids inside the disk are shown by small circles in Fig. 2; this is a disk of small bubbles; disk plane is perpendicular to the axis L of a laser beam. The nucleation disk is a spatial zone around beam axis L where nucleation of voids takes place. Near nucleation threshold, this disk is placed at the depth $d_{crat}|_{abl}$ under surface. It is very important that at our conditions with ultrafast lasers and metals, the ablation threshold F_{abl} is higher than melting threshold. Therefore nucleation takes place in molten material. The curve m–c in Fig. 2 marks a front of melting and re-crystallization.

Due to expansion of heated matter, the vacuum boundary 1 in Figs. 1 and 2 moves in the normal direction x; compare current position 2 of the boundary with its initial position 1 in Fig. 2. Radial and normal extensions of a nucleation zone increase with increase of fluence $F > F_{abl}$, see Fig. 3. Radial extension of nucleation zone is proportional to R_L if we fix relative central fluence $f_c = F_c/F_{abl}$. Normal (along x) extension increases when value f_c increases; of course, at a fixed radial position and fixed radius of a beam. In the shallow case $d_T < < R_L$, normal extension does not depend on R_L. In the shallow case, instant extension of nucleation zone along x depends on time passed after fast irradiation and on local value of normalized fluence $f = F/F_{abl}$.

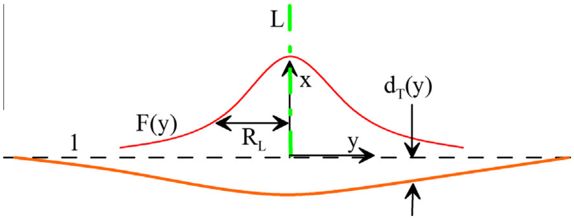

Fig. 1. Initial position of the target-vacuum boundary is the dashed line 1. Prior to a laser shot, target material was below the line 1; $F(y) = F_c \exp(-y^2/R_L^2)$ [J/cm^2] is a fluence distribution around the axis L of a laser beam; d_T is thickness of a layer heated by laser.

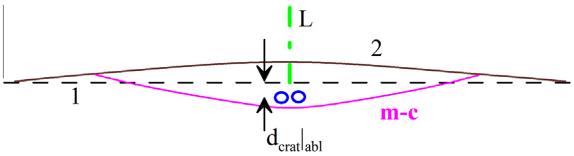

Fig. 2. Nucleation of voids inside of molten layer in case with fluence near threshold F_{abl}. The plane 1 is an unperturbed surface; the curve 2 shows instant position of a target surface in its expansion motion after irradiation. The depth $d_{crat}|_{abl}$ corresponds to the depth of future crater, since near the ablation threshold voids nucleate only near bottom of a crater.

The function $d_{spall}(y)$ in Fig. 3 gives a thickness of a spallation layer. This layer forms a shell or cupola like roof above a vapor–liquid mixture. The mixture fills lens like volume in Fig. 3. The spallation layer consists of continuous liquid, contrary to the two-phase lens. The spallation cupola and two-phase lens are in motion. For fluencies above ablation threshold, they expand up in Fig. 3 in their motion. The function $d_{spall}(y)$ has minimal value in the central point $y = 0$ since local value of fluence has maximum in this point, see Fig. 1. Expansion velocity is maximal in the center. The function $d_{spall}(y)$ depends on local fluence $F(y)$ in point $y - d_{spall}(F)$, $d_{spall}[F(y)]$, $d_{spall}(y)$. The function $d_{spall}(F)$ monotonically decreases as fluence increases. Obviously, there is a definite value of fluence F_{ev} (the threshold for disappearance of spallation layer) when a hole $d_{spall}(y = 0) = 0$ in a spallation shell $d_{spall}(y)$ appears; the disappearance threshold F_{ev} is higher than ablation threshold: $F_{ev} > F_{abl}$.

Figs. 1–3 describe principal features of the thermo-mechanical ablation. As was said, ablation means removal of matter from target as a result of irradiation. In case of short pulse lasers the thermo-mechanical ablation gives dominant contribution into amount of removed mass. In this case a surface layer of mass is ablated by mechanical separation from target. This process is similar to spallation.

2. Undersurface frozen bubbles

Let $f_c = F_c/F_{abl}$ is slightly above 1 and radius R_L is large enough in comparison with depth d_T. In this situation the spallative run-away of the spallation shell $d_{spall}(y)$ in Fig. 3 follows through decay of lateral walls between neighbor cavitation bubbles shown in Fig. 4 and coalescence of these bubbles into large void which separates the shell $d_{spall}(y)$ from the rest of a target. After creation, the voids increase their volume during run-away of the shell. The shell totally separates from a target in the region of a lateral wall $r = y_{abl}$ of a future crater. In left panel of Fig. 4 a chain of bubbles after nucleation but prior to coalescence is shown. Large oblate ellipsoid in left panel of Fig. 4 is formed due to coalescence of central small bubbles. Lateral walls of this ellipsoid are the future lateral walls of a crater.

Cavitation bubbles evolve inside a molten layer which gradually cools and freezes during and after the process of spallation shell separation from a target. The bubbles near the crater wall have a chance to keep frozen if cooling process is fast enough to leave behind the contraction and collapse of bubbles under action of surface tension. Bubbles near the crater walls are shown in Fig. 4 (right). The two processes – one of bubble inflation and second of bubble contraction – compete with each other. Inflation of bubbles takes place during deceleration of the spallation shell [1,2,5]. Surface tension resists to the run-away of a shell and maintains deceleration of a shell. Surface tension begins to work for bubble contraction after separation of the spallation shell. The lateral (in respect to a ctater) bubbles survive near the lateral walls of a crater, see right panel of Fig. 4, where these lateral bubbles are shown.

As was said, the spallation shell is a cover or a roof above a cavitation zone in Fig. 3 or above a large oblate void in left panel of Fig. 4. If absorbed fluence is above ablation threshold $f_c = F_c/F_{abl} > 1$ then the cover runs-away. The run-away opens a central void and transforms this initially closed void in left panel of Fig. 4 into a well in right panel of Fig. 4. This well in a target is called a crater. Matter, which has filled the well, constitutes the spallation shell if normalized central fluence f_c is slightly above 1. If the fluence f_c is significantly higher than one, then part of matter from a crater constitutes the spallation shell while another part constitutes vapor–liquid and vapor ejecta. The rim around the lateral wall corresponds to a near-threshold region $F(y) \approx F_{abl}$. Small voids near the lateral wall in right panel of Fig. 4 may blow out, or remain frozen, or collapse and disappear. The broken small bubble “g” together with frozen one “h” is shown in Fig. 5. They locate inside the rim. If “g” is a broken small void, then “a” is a broken large void shown as an oblate ellipsoid in Fig. 4 (left).

An image of topography of a laser crater on aluminum surface is shown in Fig. 6. This image has been obtained by focused ion beam (FIB) operating in low current regime. Ion beam produces secondary electrons collected by imaging system of an

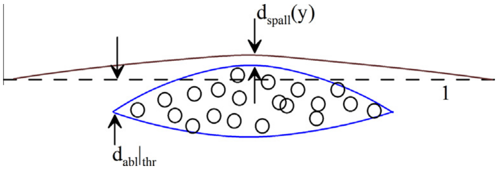

Fig. 3. Above ablation threshold the nucleation zone is the radially (that is along y) elongated volume with voids. The line 1 is initial boundary of target.

Fig. 4. Process of caviation and spallation: multiple nucleation in the horizontally elongated layer under the spallation shell $d_{spall}(y)$ is shown in left panel; merging of small bubbles in the central region of the horizontally elongated layer of bubbles into the large void shown by oblate ellipsoid (left); run-away of the spallation shell $d_{spall}(y)$ and formation of the crater with sharp lateral walls (right); the walls correspond to the circle $r = y_{abl}$ where fluence achieves the threshold $F_c \exp(-y_{abl}^2/R_L^2) = F_{abl}$; dashed line is an initial boundary.

electron microscope. FIB in low current regime is a rival to the more familiar scanning electron microscope (SEM) in terms of imaging topography. Fig. 6 presents a frontal view along the axis L normal to a plane of initial boundary, see Figs. 1, 2 and 5. Cr:forsterite laser pulse parameters for this shot are: duration 100 fs, wavelength 1240 nm, 45° is angle of incidence, $R_L = 25$ µm, $f_c = 1.05$. FIB image in Fig. 6 clearly shows details of an irradiated spot: the crater, the lateral wall of a crater, and the rim around the wall. This is a final image obtained much later (half a year later) after termination of all processes initiated by laser shot. The spallation shell, which covers the crater, has run away. The inner rim connected with lateral wall is the place where separation of the cover from target has took place; see Fig. 5 which illustrates fracture of bonds between the shell and the target. The main rim, located outside to the wall, experienced near threshold irradiation but has kept connection with a target. Surface structures in the rim and at the bottom of crater are obviously different.

There are traces of broken small bubbles in the rim. Some of them are shown in Fig. 6 (left panel).

As was said above, the spallation shell covers association of small bubbles, while the left panel in Fig. 6 shows small craters corresponding to the individual small cavitation bubbles similar to the broken bubble "g" in Fig. 5. The relief of surface in the rim has traces of knobs. It is suspicious that this relief hides frozen nanobubbles like bubble "h" shown in Fig. 5.

FIB image reveals fine details of structures created by laser pulse. This is important advantage. While great advantage of micro-interferometric technique is ability to measure the depths of extremely shallow structures, see profile of the crater in Fig. 7. Technique, used to obtain micro-interferometric image shown in Fig. 7, is described in paper [5], see also references given in this paper.

As was said above, region of the rim in Fig. 6 is suspicious. It may contain nanobubbles hidden under target boundary. To check this suggestion, we use combination of focused ion beam (FIB) and transmission electron microscopy (TEM) (Lamella technique [6,7]). A thin slice, crossing the crater wall and rim shown in Figs. 6 and 7, was, first, covered by protective layer of platinum metal-organic and, second, was cut out from aluminum film. The slice crosses the rim in radial direction. The metal–organic layer covering the surface structures protects them from ion milling. Target shown in Figs. 6 and 7 is an aluminum film deposited onto glass plate. The obtained slice has been separated from glass plate and has been transferred to TEM.

The TEM image of the obtained slice is shown in Fig. 8. In Fig. 8 the dark granulated layer on the top of Al surface is the platinum protective layer. We see that the nanobubbles form a layer under Al surface. The bubble layer thickness is 50–100 nm.

3. Frozen broken foam in the bottom of a crater

Ultrashort laser pulses (ULP) produce thermo-mechanical (TM) stress at an acoustical time scale. Such stresses (in combination with freezing process) are the reason for creation of frozen nano-bubbles (if $F \approx F_{abl}$, Fig. 8) and frozen disrupted foam ($F > F_{abl}$, Figs. 9 and 10). Results of irradiation by optical and X-ray ULP are similar in terms of production of TM stress,

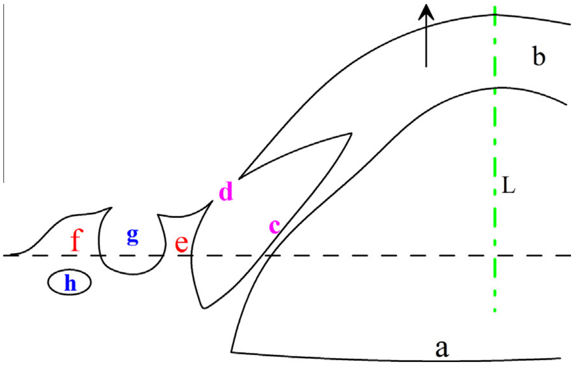

Fig. 5. Breaking of bonds "c" and "d" connecting the spallation shell "b" and a target. The circle of the lateral wall is the place of connection between the shell and the target. This is a circle if we look at the irradiated focal spot shown here from above. The shell run-away in normal direction is shown by the arrow. The bonds decelerate runaway motion of the shell. The "e", "f" is an elevated rim around a wall. The rim is elevated above initial boundary shown by dashed line; "a" is a bottom of crater. The elevations "e", "f" are caused by expulsion of matter out from a set of the undersurface voids similar to the void "h".

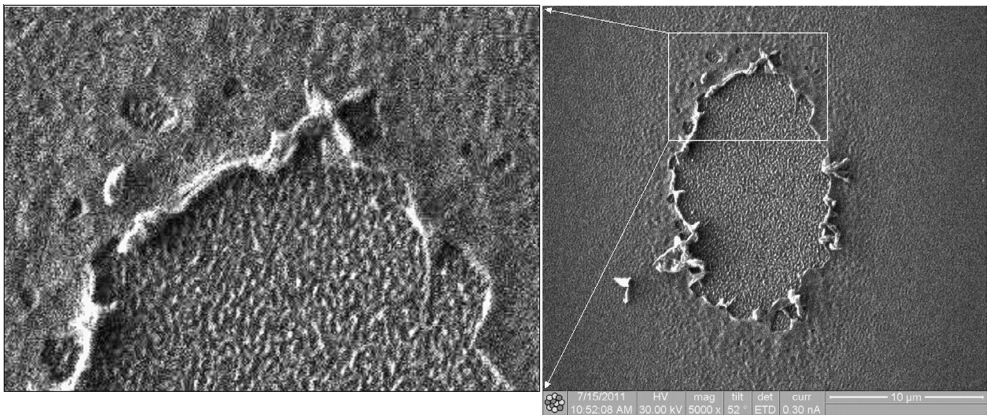

Fig. 6. Crater and a rim produced by a single optical laser shot. Crater has an elliptical form because target has been illuminated by inclined laser beam.

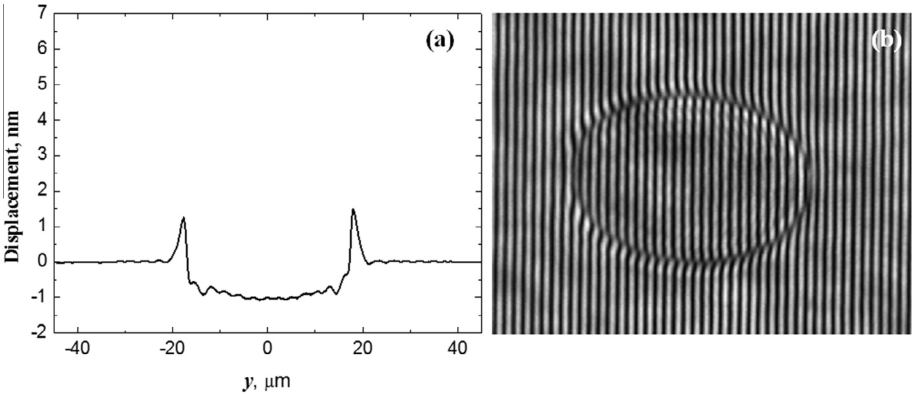

Fig. 7. (a) Final profile of crater and rim at an aluminum target obtained from the micro-interferometric image shown in the right panel. These image and profile correspond to the crater shown in Fig. 6. (b) Final micro-interferometric image of crater and rim around.

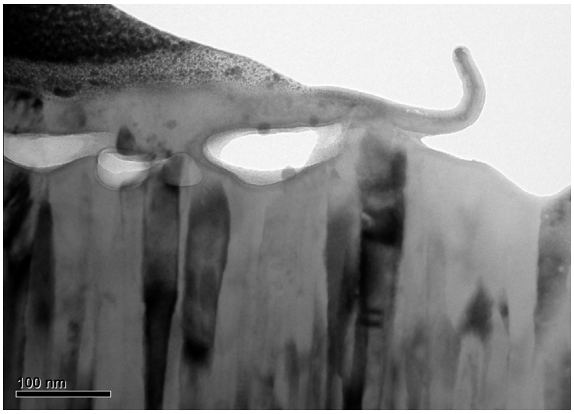

Fig. 8. TEM image of a thin slice milled by FIB. The image reveals existence of frozen bubbles beneath the surface of Al film in the rim around the crater. The rim belongs to near-threshold region.

in spite of the physics of light absorption varies qualitatively. Therefore optical and X-ray ULP both generate nano-deformed structures with frozen bubbles and foam.

Let us consider the case above threshold $F > F_{abl}$. There are multiple nucleations in a spatially extended region. New and new layers of cavitation bubbles are created as a stretching wave penetrates deeper into target; see paper [8] and .avi fails attached to the supplement of this paper. Formation of an ensemble of cavitation bubbles is accompanied by stretching of this ensemble due to inertial expansion of two-phase (vapor–liquid) mixture. Indeed, the mixture has been accelerated to some finite velocity and as a result of inertia the mixture cannot be stopped at once, expansion of mixture continues with velocities which gradually decrease in time. The decrease is caused by resistance of foam to stretching; see discussion concerning deceleration in Sections 1 and 2 above. The stretching of a mixture gradually decreases the volume fraction of liquid V_{liq}/V in the two-phase mixture; here $V = V_{liq} + V_{vap}$ is volume of mixture composed from liquid, occupying volume V_{liq} inside volume of mixture V, and vapor, occupying volume V_{vap}. During stretching, the mixture evolves from (A) small bubbles in molten matter at small values of fraction V_{vap}/V to (B) the foam state when liquid content contained in liquid walls is a small fraction of mixture: $V_{liq}/V \ll 1$. Finally at the stage (C) an expanding cloud of liquid droplets in vapor forms.

There are the A–C stages listed above. Transition between the stages B and C from isolated bubbles to isolated droplets is carried out by gradual rupture of walls surrounding the inflated bubbles. It is gradual in the sense that the rupture of walls in the upper layer of bubbles takes place first. After that the next, deeper layer of walls decays. The up and down directions are as in Figs. 1–5 where the axis *x* is shown. As time progresses, the more and more deep layers of walls decay. There is a "front" of the decays propagating from the outer surface into the bulk of a target. Above the front there is percolation through vapor in the two-phase mixture, while below the front there is percolation through liquid.

Gradually the front of ruptures comes near and near to the bottom of the future crater. There are two converging fronts: the front of decays of liquid walls coming from the outer surface and the recrystallization front "m-c" (see Fig. 2) separating melt and poly-crystal. The latter front moves up in Figs. 1–5 along the axis *x* from the side of bulk target.

X-ray pictures on Nickel (Fig. 9) and gold (Fig. 10) have been obtained at Ag plasma laser [9–16]. Intensity distributions are rather stable from shot to shot. Luminescence of color centers of irradiated LiF [9] has been used to define intensity distribution across the irradiated spot, see the upper left corner in Fig. 9. Qualitative reasons for appearance of frozen structures now are well established [9,11,12]. At the same time, there is still unclear why threshold on absorbed energy in the X-ray case is significantly below than the threshold in case of optical lasers acting on absorbing targets (in case considered here, there are metals), see the bottom right corner of Fig. 9 where threshold for Nickel is 10–17 mJ/cm^2, while for optical irradiation of Nickel the absorbed fluence at the ablation threshold is 140 mJ/cm^2 [17].

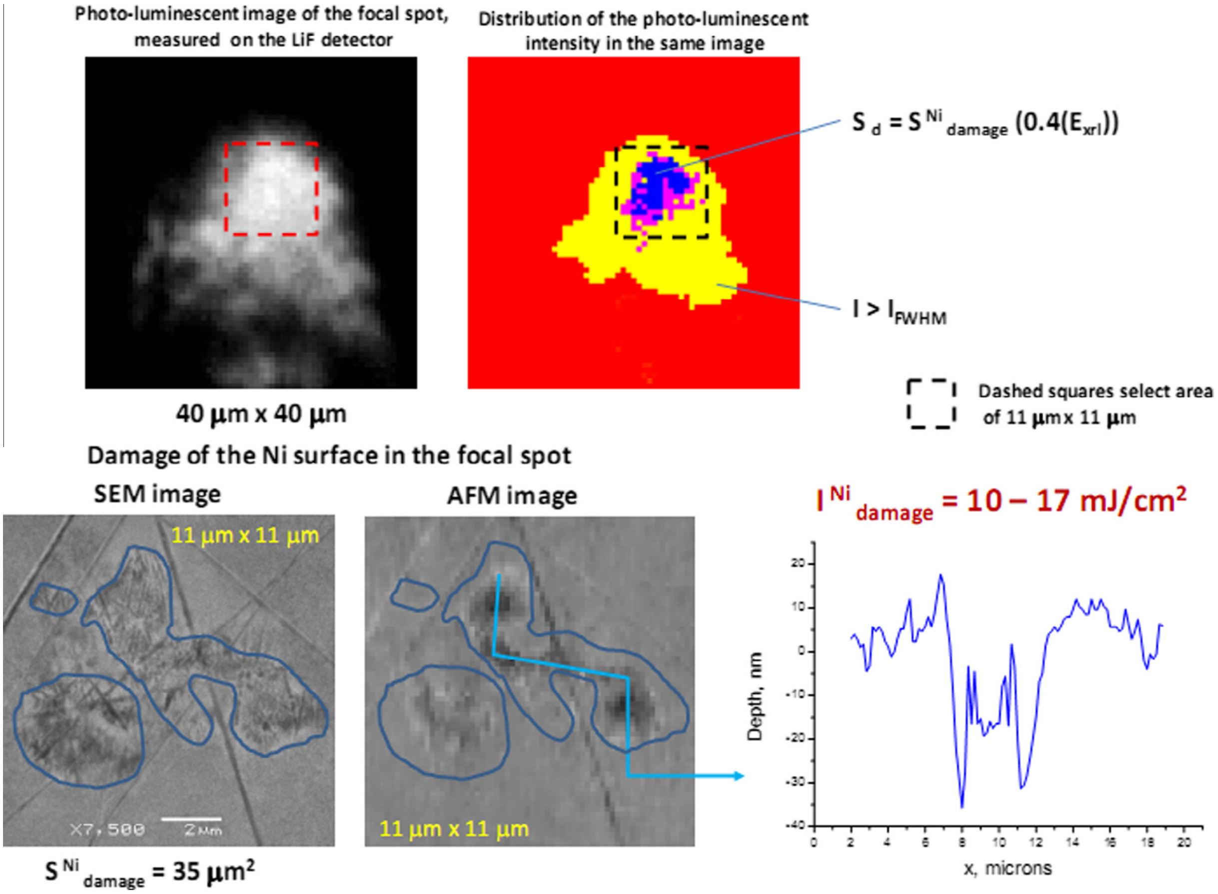

Fig. 9. Photo-luminescent (PL) image obtained at Lithium Fluoride (LiF) crystal; distribution of intensity according to the PL image; SEM image; AFM image; and the AFM damage profile, showing ablated depth inside the irradiated spot.

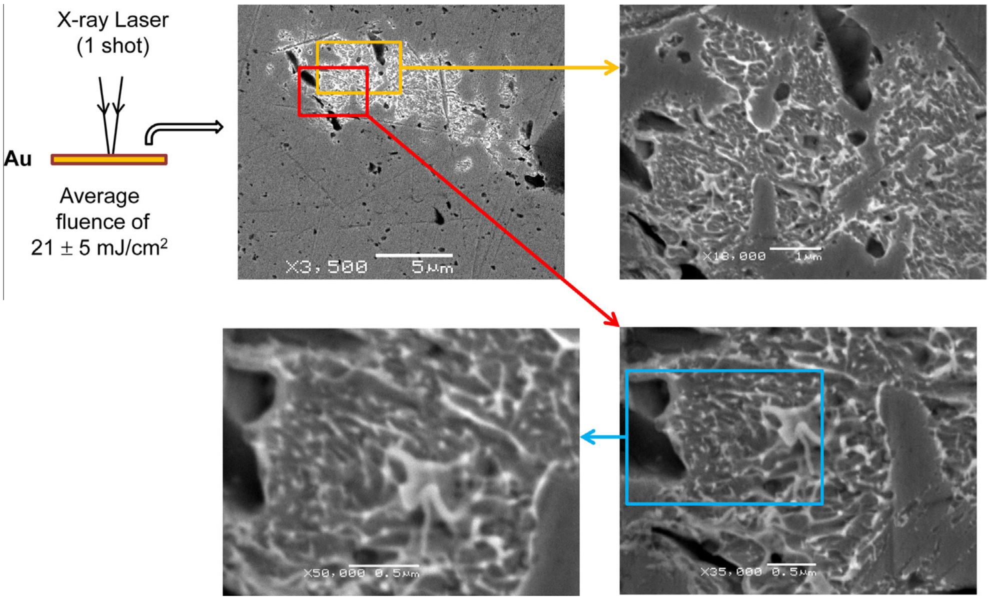

Fig. 10. Clear evidence of existence of frozen nano-foam structures after single X-ray shot.

4. Defects created by foaming and solidification and defect layer leaved by plastic shock

As was said above, foaming/solidification play important role in formation of surface nanostructures. Our large scale molecular dynamics (MD) simulations [5] show that at late stage, when solidification proceeds via non-equilibrium crystallization, newly formed metallic solids include dense dislocation net and high concentration of vacancies. The late solidification stage begins at distances ~10 nm near the transit between inner part of foam and continuous melt. Especially small nano-crystallites form during freezing of the liquid walls and jets. These walls are pieces of planes. The planes separate neighbor bubbles in foam, and form Voronoi like 3D mesh of polyhedron bubbles. Voronoi like internal structure of foam forms when volume fraction of molten metal in two-phase liquid–vapor mixture drops to small values. Nano-crystallites grow from free surface of walls and even inside bulk melt because overcooling temperatures achieve large values – few hundreds of Kelvins below melting temperature. In those conditions the defect layer, formed by fast re-crystallization, is subdivided into two sublayers – one is the near surface layer in continuous medium, while another sublayer is formed by solidified walls and jets. In the last sublayer ultimate concentration of defects is achieved.

At non-equilibrium stage velocities of re-crystallization front ($u_{cryst} \sim 10$–100 m/s) drops significantly below values corresponding to solution of Stefan problem [5,18–20]. These velocities are diffusion limited. Fast re-crystallization with maximum possible velocity u_{cryst} and the diffusion limit are responsible for formation of Frenkel pairs decaying into vacancies [20] (interstitials have large mobility and diffuse into liquid). Similar results concerning increase of defect concentration in direction to foam has been reported recently [20]. Very large scale MD simulations, mentioned above, are necessary since, first, crystallization proceeds slowly and simulation during long period of time ~ nanosecond is necessary, and, second, since lateral dimensions in 3D are huge for MD simulations (~100–1000 interatomic distances). Lateral dimensions should cover few typical average lengths $\langle l \rangle$ between nanostructure elements.

Above we have presented the defect layer formed by fast re-crystallization – the first layer. Its surface sublayer is tightly connected with solidification of foam. The re-crystallized layer adjoins to another defect layer leaved near surface by strong plastic shock – the second layer. The defects produced by shock are located at larger depths. They are dislocations created as a result of plastic transformations behind strong shock. As it is follow from our MD simulations [21–23], the plastic shock appears at absorbed laser fluencies F_{abs} significantly above ablation threshold, see Fig. 11. Plastic shock, generated by ultrashort laser pulse, decreases in its amplitude, as a shock propagates from surface into bulk. The decrease is steep and soon plastic shock decelerates down to subsonic velocities and stops. The depth of stopping depends on absorbed energy F_{abs}: larger energy – larger stopping depth. Strong shock propagates as elastic shock at depths larger than the stopping depth. It uniaxially compresses crystal. Rarefaction, following shock, drops compression stress. After that unloaded metal returns to its state prior to compression. Therefore the stopping depth defines thickness of the second defect layer.

5. Discussion

In the paper above we have considered formation of chaotic nanostructures due to foaming/freezing. Average scale of structures $\langle l \rangle$ along a surface is of the order of heated layer thickness d_T. The thickness d_T is from few tens of nanometers

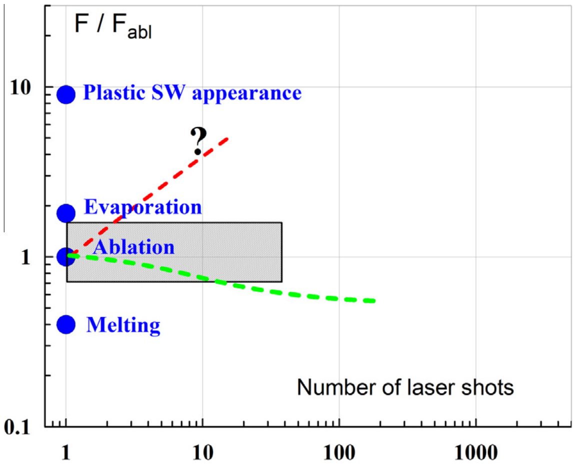

Fig. 11. Sequence of (1) melting, (2) ablation, (3) evaporation, and (4) plastic shock thresholds for ultrashort optical and X-ray laser irradiation. Positions of circles correspond to the case of a single laser shot. Typical for metals positions are shown. Below the melting threshold target remains solid during and after illumination. Spallation layer detaches from target above the ablation threshold. Spallation layer disappears above the evaporation threshold. Below the plastic shock wave (SW) threshold, the laser pulse produces only elastic SW. SWs propagate from irradiated surface into bulk. Plastic SW appears above the fourth threshold. The rectangular shows region of fluencies and numbers of shots studied in X-ray laser experiments [23]. There are no surface structures below the green dashed curve. There are no ripples above the red dashed curve. (For interpretation of the references to colour in this figure legend, the reader is referred to the web version of this article.)

and up to of order of one hundred nanometers depending on material. Let's give some general remarks concerning comparison of foaming/freezing mechanism versus mechanism based on interference between incident electromagnetic laser wave and surface plasmons [25–28]. The last mechanism operates only in the case of infrared and optical lasers. Surface plasmons frequencies are much softer than soft X-ray frequencies; therefore we can exclude their influence for the cases with illumination by hard photons. In the case of optical lasers primarily ripple structures appears with ripple direction perpendicular to polarization of electromagnetic wave [25–28]. Although other structures are also observed (cellular, double ripples, irregular). It is significant, that step of ripples (ripple space period) should be of the order of laser wavelength λ [25,26] because this is a spatial period of surface plasmons in resonance with incident wave. Observed structures often have periods more close to the thermal length $d_T \cong 100$ nm than to the infrared or optical wavelengths $\lambda \cong 1000$ nm.

Similar ripples are observed in experiments with long pulse (nanoseconds) lasers [29]. In the nanosecond case mainly thermal effects are important; evaporation or sublimation become significant. There are no tensile stresses and undersurface cavitation in this case. Ripples are also produced by action of ion beam (ion sputtering) [30]. Some times investigators mention that there are similarities with sand ripples (sand dunes). The dunes are oriented perpendicular to wind direction.

From one side, Fig. 11 has been designed to emphasize existence of four thresholds for single shot irradiation by ultrashort laser pulse. Those thresholds relate to described above thermal and mechanical phenomena induced by ulrashort laser pulse. From the other side, Fig. 11 has to illustrate our discussion concerning relative roles of foaming/freezing and plasmon mechanisms in formation of surface structures. There are regions where one or another mechanism dominates, and regions where hybridization of both combines them into unified process producing structures. Indirect confirmation of presence of thermal processes may be taken from the fact that the scales smaller than thermal depth d_T are not observed. This simply follows from a smoothing action of electron heat conductivity playing very important role in formation of a surface heated layer.

Nucleation threshold F_{nucl} is close to ablation threshold F_{abl} but it is 2–10% below F_{abl} [1,2,5]. In the interval $F_{nucl} < F < F_{abl}$ cavitation nuclei appear but they cannot separate spallation plate. Below thresholds F_{nucl}, F_{abl} mechanical aspect is of little significance while thermal effects (formation of hot layer, melting/crystallization) remain. There are linked thermal and mechanical actions (thermomechanics) above those thresholds. Thus contribution from foaming/freezing into formation of surface structures is possible only above thermomechanical thresholds F_{nucl}, F_{abl}.

There is significant reflection of light in case of infrared and optical lasers. Absorption coefficient $A = 1 - R$ is very small (few percents) for some metals and depends significantly on surface properties (roughness, contamination); also, obviously, a coefficient A depends on wavelength, inclination, and polarization. Therefore incident F_{inc} and absorbed $F_{abs} = AF_{inc}$ energies are different. It is clear that exactly definite amount of absorbed energy is necessary to detach spallation layer. Therefore an ablation threshold relates to absorbed fluence. In our optical ablation simulations operating with absorbed fluence, corresponding incident fluence should be defined separately (it may be different at the same F_{abs} depending on inclination, polarization and so on). In experiments special attention should be made to define absorbed energy after every of successive shots into the same spot. This is so since absorption coefficient A may be changed after every shot. Indeed, phenomenon of metal colorization (e.g., "black gold") is observed in remarkable experiments [31]. This is linked to changes in optical parameters of surface. The parameters change because surface structures are deforming and growing from shot to shot. If we do not know absorbed energy after shot number N, than we do not know where the point corresponding to this shot is on the plane N, $F_{abs}/(F_{abs})_{abl}$. This plane is shown in Fig. 11. Important point 1, 1 in Fig. 11 presents absorbed fluence normalized relative to ablation threshold on absorbed fluence after single shot.

We believe that after a single shot onto well polished and clean metallic target, ablation threshold is defined only by thermomechanical processes – we can neglect influence of plasmons. This is so because surface non-homogeneities should be present [2] during pulse to excite plasmons. Indeed, heating laser pulse is so short in time that irradiated surface remain unmoved during pulse for our range of fluencies (moderate fluencies). Therefore absorbed fluence is homogeneously distributed along a well polished surface. We believe that nanostructures, formed after single shot, are formed through foaming/freezing mechanism. Those structures start from thermal fluctuations and nucleation and are chaotic. But now there are experimental papers where authors have observed ripples after single shot [32,33]. In paper [33] the ripples are directed perpendicular to polarization, in [32] direction of polarization was not defined. Maybe there was significant initial surface roughness in those experiments which seeds resonant surface plasmons?

As was shown in the paper, after the first short ($N = 1$) the surface non-homogeneities appear if absorbed fluence is above nucleation threshold F_{nucl}. Those non-homogeneities change absorption coefficient A – this coefficient becomes a functional $A\{\eta(y,z)\}$ depending on relief of a surface $x = \eta(y,z)$; direction of normal and tangential axes are shown in Fig. 1; the scale $\langle l \rangle$ of inhomogeneities is of the order of thermal depth d_T. Therefore a distribution of energy per surface unit, absorbed during the second short ($N = 2$), becomes non-homogeneous, contrary to homogeneous illumination by incident beam (typically beam radius is much larger that wavelength). This is caused by changes of inclinations and optical parameters of a surface from point to point and by excitation of surface plasmons at a non-homogeneous boundary.

Thus, the second shot amplifies non-homogeneities since there is non-homogeneous heating. Let us consider linear polarized incident optical laser wave. Non-homogeneities produced by shot $N = 1$ have wide spatial spectrum, isotropic relative to directions relative to tangential wavevectors k_y, k_z. The plasmon interference amplification selects wavevectors corresponding to amplifying modes of surface plasmons. This induces gradual (from shot to shot) amplification of ripples perpendicular to polarization.

Usually in experiments the incident fluence F_{inc} is fixed and number of shots N is gradually increased. Time intervals between shots are long enough to cool an illuminated spot down to room temperature. In Fig. 11 the vertical axis correspond to normalized absorbed fluence $\bar{f}_{abs} = F_{abs}/(F_{abs})_{abl}$. The bar sign above the normalized absorbed fluence means that this is fluence averaged along the inhomogeneous surface. Due to growing of surface perturbations, the absorption A coefficient increases. Therefore the sequence of points $(N,\bar{f}_{abs})$, $N = 2,3,\ldots$ in the plane $(N,\bar{f}_{abs})$ deviates up from a horizontal straight line (F_{inc} is fixed), as number N increases.

Function $\Delta\bar{f}(N)$, giving deviation up from the horizontal line, depends significantly on the height $\bar{f}_{abs}$ of the straight line above the axis N. The deviation $\Delta\bar{f}(N)$ (F_{inc} is fixed) grows fast with N if $\bar{f}_{abs} > 1$ since above the ablation threshold the strong inhomogeneities remain on a surface after irradiation. Average thickness of ablated layer $h_{abl} \sim 20$–100 nm (particular value depends on metal) per one laser shot is large for fluencies above the threshold $\bar{f}_{abs} > 1$. Below this threshold, ablated thickness h_{abl} is much smaller; it is $\sim$1 nm, one atomic monolayer or less; here the mechanism of ablation is evaporation or even sublimation below melting threshold or after re-crystallization of molten layer. Therefore (smallness of h_{abl}) accumulation of inhomogeneities proceeds very slowly with increasing of number N. Many shots are necessary to produce ripples at low fluencies. The green dashed curve in Fig. 11 presents threshold for formation of surface structures. There are no structures below this curve.

Red dashed curve above and green dashed curve below outline a region in Fig. 11 where plasmons and interference are important contributors into process of structure formation under optical excitation. As was said, the line $\bar{f}_{abs} \approx 1$ divides this region into sub-regions of active and passive motions. The red curve is poorly understood. This is emphasized by the sign "?" in Fig. 11. At high fluencies $\bar{f}_{abs} >> 1$ thick layers h_{abl} are ejected out of target after every shot. The heights of structures have amplitudes comparable with ablated thickness h_{abl}. It seems that this process (removal of thick layers) impedes to adjust lengths suitable for interference of coherent incident laser light with plasmons (interference or coherence between laser and plasmons along large $>> \lambda$ surface area). But plasmons itself are present locally even during the second shot, because after a shot number $N = 1$ the strong surface inhomogeneities are created. Surface shape $x = \eta(y,z)$ becomes complicated (see examples in Figs. 9 and 10), it has narrow channels decreasing resonance frequency of plasma field oscillations down to the optical light frequency. Oscillating electric field near surface is a sum of incident plane wave and plasmon's field. There are significant inhomogeneous amplifications above an average level of intensity of laser incident filed. The spots of amplification locate around narrow channels. More energy per unit surface is absorbed in those spots. Distances between the spots define average scales $\langle l \rangle$ of the structures growing with number of shots N .

Figs. 9 and 10 present X-ray single shot experiments with Ni and Au, resp. Photon energy is 89.3 eV, wavelength is $\lambda = 13.9$ nm. There are clear indications in Fig. 10 that foaming and freezing are responsible for formation of observed structures. Statistical spread of scales $\langle l \rangle$ $\sim$0.1–0.5 μm is large. Attenuation depth for gold is 19 nm for these photons. Our simulations [8] show that thermal depth for gold is $d_T \approx 140$ nm. Evolution of structures with increase of number of shots N up to $N = 20$ has been studied in paper [24]. Observations [24] show that scales $\langle l \rangle$ increase in length with number N few times up to $\langle l \rangle$ $\sim$1 μm.

X-ray fast oscillating field cannot excite plasmons. Also from forms of structures shown in Fig. 10 it follows that we are in sub-region of active motions above ablation threshold in Fig. 11. Therefore it is not surprising that structures are chaotic and we do not see in [24] any traces of arranging of surface perturbations into ripples.

6. Summary

The main goal of this paper is to emphasize that the frozen nano-structures created by single ultrashort pulse of optical or X-ray lasers are similar. These structures are linked to thermo-mechanical stress and to creation of pressurized surface layers existing during acoustic time scale near irradiated surface. Theory of the thermo-mechanical ablation by X-ray short pulse has been developed in papers [9–11]. Here we present basements of these theories and supporting experimental data.

Acknowledgement

Authors (M.B.A, N.A.I, V.V.Zh, S.I.Ash, V.A.K, Yu.V.P) acknowledge support from RFBR Grant No. 13-08-01095.

References

[1] Zhakhovskii V, Inogamov N, Nishihara K. J Phys: Conf Ser 2008;112:042080.
[2] Zhakhovskii VV, Inogamov NA, Nishihara K. JETP Lett 2008;87(8):423.
[3] Sokolowski-Tinten K, Bialkowski J, Cavalleri A, von der Linde D, Oparin A, Meyer-ter-Vehn J, et al. Phys Rev Lett 1998;81:224.
[4] Inogamov NA, Petrov YuV, Anisimov SI, Oparin AM, Shaposhnikov NV, von der Linde D, et al. JETP Lett 1999;69(4):310.
[5] Ashitkov SI, Inogamov NA, Zhakhovsky VV, Emirov YuN, Agranat MB, Oleinik II, et al. JETP Lett 2012;95(4):176.
[6] Giannuzzi L, Stevie FA, editors. Introduction to focused ion beams: instrumentation, theory, techniques and practice. Springer; 2005.
[7] Mayers J, Gianuzzi L, Kamino T, Michael J. MRS Bull 2007;32(5):400.
[8] Demaske BJ, Zhakhovsky VV, Inogamov NA, Oleynik II. Phys Rev B 2010;82:064113.
[9] Faenov AYa, Inogamov NA, Zhakhovskii VV, Khokhlov VA, Nishihara K, Kato Y, et al. Appl Phys Lett 2009;94:231107.
[10] Cherednikov Y, Inogamov NA, Urbassek HM. J Opt Soc Am B 2011;28:1817.
[11] Inogamov NA, Faenov AYa, Khokhlov VA, Zhakhovskii VV, Petrov YuV, Skobelev IYu, et al. Contrib Plasma Phys 2009;49(7–8):455.
[12] Inogamov NA, Zhakhovsky VV, Faenov AY, Khokhlov VA, Shepelev VV, Skobelev IY, et al. Appl Phys A 2010;101(1):87. arXiv:0912.3184.
[13] Ishino M, Faenov AYa, Tanaka M, Hasegawa N, Nishikino M, Tamotsu S, et al. J Appl Phys 2011;109:013504.
[14] Inogamov NA, Faenov AYa, Zhakhovskii VV, Skobelev IYu, Khokhlov VA, Kato Y, et al. Contrib Plasma Phys 2011;51(4):361.
[15] Inogamov NA, Faenov AYa, Zhakhovsky VV, Pikuz TA, Skobelev IYu, Petrov YuV, et al. Contrib Plasma Phys 2011;51(5):419.
[16] Inogamov NA, Anisimov SI, Zhakhovsky VV, Faenov AYa, Petrov YuV, Khokhlov VA, et al. Proc SPIE 2011;7996:79960T.
[17] Inogamov NA, Petrov YuV, Zhakhovsky VV, Khokhlov VA, Demaske BJ, Ashitkov SI et al. In: International symp. High power laser ablation, AIP Conf. Proc. vol. 1464, 2012. p. 593–608.
[18] Chan W-L, Averback RS, Cahill DG, Ashkenazy Y. Phys Rev Lett 2009;102:095701.
[19] Karim ET, Lin Z, Zhigilei LV. In: Internat. symp. on high power laser ablation, AIP conf. proc. vol. 1464, 2012. p. 280–93.
[20] Wu C, Karim ET, Zhigilei LV. Report PL3-6, <http://www.lastech.ifmo.ru/FLAMN13/PROGRAM_FLAMN13.pdf>.
[21] Inogamov NA, Zhakhovsky VV, Khokhlov VA, Shepelev VV. JETP Lett 2011;93:226–32.
[22] Inogamov NA, Khokhlov VA, Petrov YuV, Anisimov SI, Zhakhovsky VV, Demaske BJ et al., editors. Tracy vogler and mark elert. In: AIP conf. proc. shock compr. cond. matt. – 2011. AIP conf. proc. vol. 1426; 2012. p. 909–12.
[23] Demaske BJ, Zhakhovsky VV, Inogamov NA, Oleynik II. Phys Rev B 2013;87:054109.
[24] Ishino M, Faenov AY, Tanaka M, Tamotsu S, Hasegawa N, Nishikino M, et al. Appl Phys A 2013;110:179–88.
[25] Sipe JE, Young JF, Preston JS, van Driel HM. Phys Rev B 1983;27:1141–54.
[26] Akhmanov SA, Emelyanov VI, Koroteev NI, et al. Sov Phys Usp 1985;28:1084.
[27] Costache F, Kouteva-Arguirova S, Reif J. Appl Phys A 2004;79:1429.
[28] Ionin AA, Kudryashov SI, Makarov SV, Seleznev LV, Sinitsyn DV, Ligachev AE, et al. Laser Phys Lett 2013;10:056004.
[29] Makin VS, Pestov YuI, Privalov VE. J Opt Technol 2013;80(2):91.
[30] Reif J, Varlamova O, Varlamov S, Bestehorn M. Appl Phys A 2011;104:969–73.
[31] Vorobyev AY, Guo C. J Appl Phys 2011;110:043102.
[32] Gurevich EL. Phys Rev E 2011;83:031604.
[33] Ionin AA, Kudryashov SI, Seleznev LV, Sinitsyn DV, Emel'yanov VI. JETP Lett 2013;97:121–5.